Measurements of $A_y(\theta)$ for $^{12}C(n, n)^{12}C$ from $E_n = 2.2$ to 8.5 MeV

C. D. Roper,[1,*] W. Tornow,[1] R. T. Braun,[1,†] Q. Chen,[1,‡] A. Crowell,[1] D. Gonzalez Trotter,[1,§] C. R. Howell,[1] F. Salinas,[1,¶] R. Setze,[1,**] R. L. Walter,[1] Zemin Chen,[2] Hongqing Tang,[3] and Zuying Zhou[3]

[1]*Department of Physics, Duke University and Triangle Universities Nuclear Laboratory, Durham, North Carolina 27708, USA*

[2]*Department of Physics, Tsinghua University, Beijing, People's Republic of China*

[3]*China Institute of Atomic Energy, Beijing, People's Republic of China*

(Received 16 June 2004; published 19 August 2005)

The analyzing power $A_y(\theta)$ for neutron elastic scattering from ^{12}C has been measured for 33 neutron energies between $E_n = 2.2$ and 8.5 MeV in the angular range from 25° to 145° in the laboratory system. The primary motivation for these measurements is the need for an accurate knowledge of $A_y(\theta)$ for $^{12}C(n, n)^{12}C$ elastic scattering to enable corrections to high-precision neutron-proton and neutron-deuteron $A_y(\theta)$ data in the neutron-energy range below $E_n = 30$ MeV. In their own right, $^{12}C(n, n)^{12}C$ $A_y(\theta)$ data are of crucial importance for improving both the parametrization of n-^{12}C scattering and our knowledge of the level scheme of ^{13}C. The present $A_y(\theta)$ data are compared with published data and previous phase-shift-analysis results.

DOI: 10.1103/PhysRevC.72.024605 PACS number(s): 24.10.−i, 24.70.+s, 25.40.Dn

I. INTRODUCTION

For various reasons, neutron scattering from ^{12}C is probably the most studied scattering process of fast neutrons from any nucleus in the neutron-energy range below 30 MeV. In applications ranging from reactor physics 60 years ago to cancer therapy and very recently to counterterrorism, accurate parametrizations of neutron elastic scattering from ^{12}C nuclei are of special interest. Aside from these more general topics, neutron scattering from ^{12}C is crucial for understanding a number of interesting phenomena. One of those more special phenomena deals with the detection of polarized neutrons. Most commonly used detectors for fast neutrons are based on organic scintillators with a ^1H to ^{12}C ratio of ∼1. The main detection process is neutron scattering from ^1H. However, double-scattering processes involving both ^1H and ^{12}C typically contribute at the 20% level to the total neutron detection efficiency. Therefore, to calculate the efficiency of neutron detectors, the differential (and total) n-^{12}C cross section is needed over a large energy range. Furthermore, especially in the resonance region between 3 and 9 MeV incident neutron-energy, data are needed in small energy steps.

The analyzing power $A_y(\theta)$ in n-^{12}C scattering comes into play when polarized neutrons are used to measure $A_y(\theta)$ in neutron-nucleus scattering. In this case, elastic neutron scattering from ^{12}C followed by a subsequent neutron-scattering process from ^1H is the process of interest. It causes an instrumental asymmetry that cannot be compensated for by standard procedures used in analyzing power experiments to cancel instrumental asymmetries. The potential importance of this double-scattering process on neutron-nucleus $A_y(\theta)$ measurements was first indicated in Ref. [1]. Later, the effect was noticed by the Wisconsin group [2], and first corrections to neutron-proton $A_y(\theta)$ data were calculated and reported in Refs. [3,4]. However, accurate corrections require the detailed knowledge of $A_y(\theta)$ in n-^{12}C scattering. Because of the lack of such data, even the most sophisticated corrections [5] were of limited and uncertain accuracy.

In the following text we report on measurements and analysis of n-^{12}C $A_y(\theta)$ data in the incident-neutron-energy range from 2.2 to 8.5 MeV. The paper is organized as follows: In Sec. II the experimental setup is described. Sections III and IV focus on the data acquisition and finite-geometry and multiple-scattering corrections, respectively. In Sec. V our results are presented and compared with previous experimental and theoretical work. Finally, in Sec. VI we summarize and conclude.

The theoretical analysis of the present data and other existing data along with R-matrix and phase-shift analyses fits will be described in forthcoming papers by Hale [6] and Chen [7], respectively.

II. EXPERIMENTAL SETUP

A. General description

The n-^{12}C experiment was conducted with the neutron-time-of-flight (NTOF) facility at Triangle Universities Nuclear Laboratories (TUNL). The main feature of this facility is a pair of heavily shielded neutron detectors for neutron cross section and analyzing power measurements [8]. Figure 1 shows an overview of the experimental setup. Each of the two main neutron detector/shield assemblies is supported by a carriage that can be rotated through scattering angles of 25° to 145° about the vertical axis of the carbon sample. Several features

*Present address: Bettis Atomic Power Laboratory, West Mifflin, PA.

†Present address: Department of Computer Science, Duke University, Durham, NC.

‡Present address: MCI, Ashburn, VA.

§Present address: General Electric Global Research Center, Niskayuna, NY.

¶Present address: MCI, Clinton, MS.

**Present address: Pearl River Community College, Poplarville, MS.

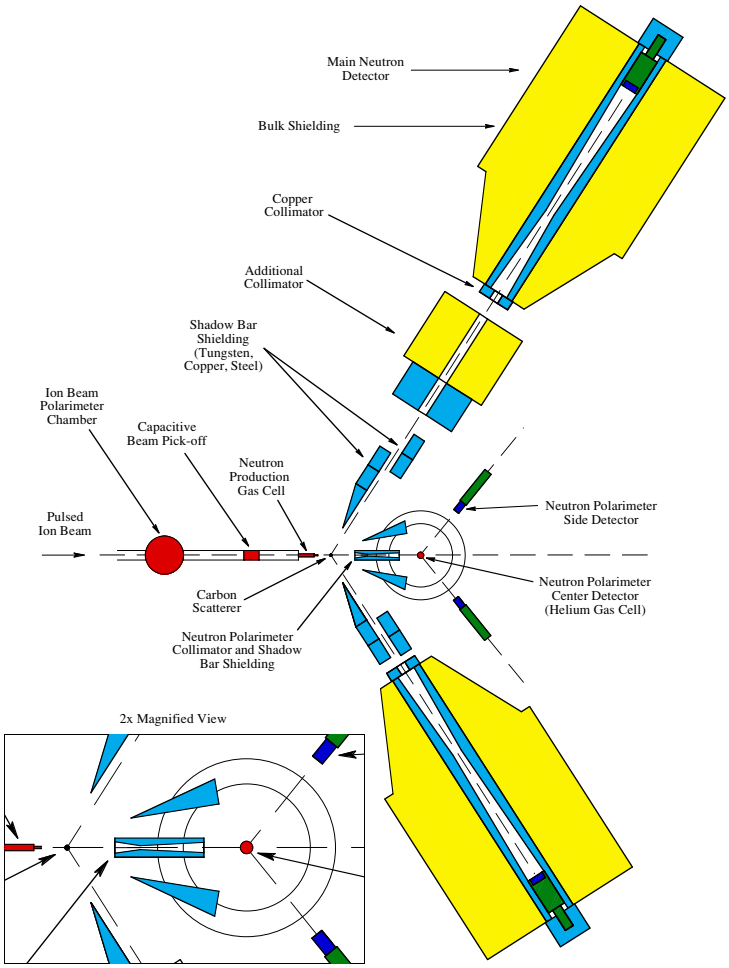

FIG. 1. (Color online) Overhead view of the TUNL NTOF facility including the charged-particle polarimeter, the capacitive beam pickoff, the neutron production cell, the carbon scatterer, the main neutron detectors, and the neutron polarimeter.

were added to the NTOF facility in order to perform the present n-^{12}C $A_y(\theta)$ measurements. A system was installed to provide neutron beam polarimetry concurrently with the n-^{12}C $A_y(\theta)$ measurements. This neutron polarimeter (NPOL), mounted downstream from the main neutron detectors, measured the polarization of neutrons transmitted through the carbon scatterer. In addition to the NPOL system, a scattering chamber for charged-particle polarimetry was inserted in the beam line upstream of the neutron production target.

B. Main neutron detectors

The neutron detectors consisted of organic liquid scintillator cells mounted to photomultiplier tubes. The scintillator cell size was 8.90 cm in diameter and 5.08 cm in depth for the right-hand detector (lower detector in Fig. 1). It was filled with Nuclear Enterprises 218. The left-hand detector (upper detector in Fig. 1) was 12.70 cm in diameter and 5.08 cm in depth and was filled with Bicron 501A. These detectors had very good pulse-shape discrimination (PSD) properties for distinguishing scintillation light produced by neutron interactions and γ-ray interactions in the scintillator fluid. The shielding surrounding each of the main neutron detectors was composed of paraffin, Li_2CO_3, copper, and lead contained in a massive cylindrical steel case. In addition to this shielding, shadow bars made of tungsten, copper, and iron were located on both sides of the scattered neutron path. These shadow bars prevented the main neutron detectors from directly viewing the neutron production source. The shadow bars also shielded the detectors from unwanted sources of scattered neutrons. The distance between the neutron detectors and the carbon scatterer was typically 3 m for the right-hand detector and 4.5 m for the left-hand detector.

C. Carbon scatterer

The carbon scatterer was 1.90 cm in diameter and 2.53 cm in height and was made of pure and natural abundance graphite. The distance from the center of the neutron production target varied between 11.93 cm for the deuterium gas cell used for the ^{2}H$(d, n)^3$He neutron source reaction and 10.48 cm for the tritiated titanium foil used for the ^{3}H$(p, n)^3$He reaction. The angle subtended by the carbon scatterer from the neutron production target was about 9°. The scatterer was supported by a thin wire at the pivot point of the main neutron detectors. The sample could be moved in and out of the neutron beam by remote control to quickly alternate between measurements with the sample in place (sample-in spectrum) and background measurements with the sample removed (sample-out spectrum).

D. Neutron beam

The polarized neutrons used for the n-^{12}C $A_y(\theta)$ measurements were produced by use of the $^3H(p,n)^3He$ reaction for neutron energies below 4 MeV and the $^2H(d,n)^3He$ reaction for neutron energies above 4 MeV. For both of these reactions the polarization transfer coefficients at 0° are greater than 0.4 in the energy range of interest [9,10]. In general, the $^2H(d,n)^3He$ reaction is preferred over the $^3H(p,n)^3He$ reaction. However, because the Q value for the $^2H(d,n)^3He$ reaction is +3.26 MeV, this reaction is not practical for neutron energies below 4 MeV.

For the $^3H(p,n)^3He$ reaction the tritium target used was tritiated titanium supported by a 0.5-mm-thick molybdenum backing foil. The tritium mass thickness was 0.09 mg/cm^2. The tritiated foil target was held by a flange to the end of a gas cell sealed with 2.5×10^{-4} cm thick Havar [11] foil from the accelerator vacuum. The gas cell was 3.2 cm long and was filled with 1 atm of ^{4}He. The purpose of the gas cell was to prevent any tritium contamination of the accelerator beam line and to facilitate cooling of the tritium foil from the inside. The outside was cooled by compressed air that was blown against the molybdenum disk. The neutron-energy was calculated with the incident-proton-beam energy, the proton-energy loss in the Havar foil, in the ^{4}He gas, and in the tritiated titanium layer. The mean neutron-energy is approximately the energy of neutrons produced at the midpoint of the ^{3}H-Ti layer. The accurate determination of the neutron-energy is described below. The neutron-energy spread is approximately equal to the proton energy loss through the ^{3}H-Ti layer.

For the $^2H(d,n)^3He$ reaction a gas cell filled with deuterium was used. The cell had a length of 3.16 cm and a diameter of 0.48 cm. It was separated from the accelerator vacuum by a 2.5×10^{-4} cm thick Havar foil. The deuteron beam was stopped in a 0.05-cm-thick tantalum beam stop at the end of the gas cell. Incident deuteron energies between $E_d = 1.28$ MeV and $E_d = 5.42$ MeV were used. The deuterium pressure in the cell varied between 0.2 and 1.5 atm and was adjusted to provide the desired neutron-energy spread for the neutron energies of interest. This pressure range corresponds to a mass-thickness range of 0.11 to 0.80 mg/cm^2. The neutron-energy was calculated with the incident-deuteron-beam energy, the energy loss in the Havar foil and in the deuterium gas. The mean neutron-energy is approximately the energy of neutrons produced at the midpoint in the gas cell. The neutron-energy spread is approximately equal to the deuteron-energy loss in the deuterium gas.

The neutrons emitted at 0° from the $^3H(p,n)^3He$ reaction are monoenergetic for the proton energies of interest ($E_p =$ 3.3 to 5.0 MeV). For the $^2H(d,n)^3He$ reaction below the deuteron breakup threshold the neutrons emitted at 0° are also monoenergetic. For $E_d > 2.23$ MeV the deuterons can break up on the Havar foil and on the tantalum beam stop of the deuterium gas cell, and for $E_d > 4.45$ MeV deuteron breakup can occur in the deuterium gas as well. Therefore, for $E_d > 2.23$ MeV, the monoenergetic neutrons are mixed with lower-energy neutrons from the deuteron breakup reactions. However, because the Q value for the $^2H(d,n)^3He$ reaction is +3.26 MeV compared with $Q = -2.23$ MeV for the highest-energy neutrons from the deuteron breakup reactions, the monoenergetic neutrons can easily be resolved from the deuteron breakup neutrons by time-of-flight (TOF) spectroscopy.

Because of the pronounced and often narrow resonances observed in the n-^{12}C total cross section, one expects the differential cross section and the analyzing power to vary drastically with incident neutron-energy. Small errors in the procedure just described for determining the neutron-energy from the incident energy of the charged-particle beams and its calculated energy loss in the neutron production target can yield significant systematic errors in the determination of the neutron beam energy. Therefore the neutron energies were calibrated empirically by use of resonances in the n-^{12}C total cross section. Because the neutron energies of these resonances are well known, one can check the calculated values for the neutron energies by measuring the n-^{12}C total cross section in the proximity of sharp resonances. In the present work the attenuation of the monoenergetic neutron beam through carbon was measured as a function of neutron-energy by use of the resonances centered at $E_n = 2.90$, 4.28, 5.37, and 6.30 MeV. With this method the neutron-energy scale was determined to an uncertainty of ±5 keV.

E. Neutron polarimeter

The NPOL, based on $^4He(n,n)^4He$ elastic scattering, consisted of a high-pressure ^{4}He gas scintillator and two neutron detectors placed in the horizontal scattering plane symmetrically about the beam axis, as shown in Fig. 1. The component of the NPOL perpendicular to the scattering plane was determined by the measured left-right asymmetry and by the known value for the n-^{4}He analyzing power [12].

The ^{4}He gas cell was a thin-walled stainless-steel cylinder 5 cm in diameter, 15 cm in height, and 1 mm in wall thickness. It was filled to 100 atm with a mixture of 95% ^{4}He and 5% Xe. The Xe was added to enhance the light output produced by the recoiling ^{4}He nuclei produced by n-^{4}He elastic scattering. The scintillation light was viewed through glass windows by a photomultiplier tube at the top and at the bottom of the cell. Details are given in Ref. [13]. The cell was positioned downstream from the carbon scatterer at a distance of 83 cm from the neutron production target.

Each polarimeter neutron detector consisted of a rectangular cell (5.0 cm wide, 12.4 cm high, and 6.8 cm deep) filled with liquid organic scintillator fluid (Nuclear Enterprises 213) and coupled through a glass window and light guide to a photomultiplier tube. These detectors were positioned at ±51° with respect to the beam axis. For this angle the figure of merit $[A_y(\theta)^2\sigma(\theta)]$ is maximized for the neutron-energy range of interest. The center-to-center distance between the ^{4}He cell and the polarimeter neutron detectors was 48.3 cm for measurements with the $^2H(d,n)^3He$ reaction and 38.5 cm for measurements with the $^3H(p,n)^3He$ reaction.

With the NPOL in place, it was physically not possible to take n-^{12}C $A_y(\theta)$ data with the two main detectors for scattering angles smaller than 45° (lab). To obtain data at smaller angles, the NPOL had to be removed. For these measurements, the vector polarization of the deuteron beam

[for the ^{2}H$(d, n)^3$He reaction] and the transverse polarization of the proton beam [for the ^{3}H$(p, n)^3$He reaction] was measured with a charged-particle polarimeter. The neutron polarization was deduced from the comparison of the charged-particle asymmetries with the measured neutron asymmetries when the ^{4}He polarimeter was in place for main detector angular settings larger than 45°. Furthermore, the spin-filter polarimeter (Ref. [14]), which is an integral part of the Atomic Beam Polarized Ion Source (ABPIS), was used to monitor the stability of the polarization of the charged-particle beams.

The neutron polarization vector was perpendicular to the horizontal scattering plane. To determine the neutron polarization from the measured n-^{4}He asymmetry, the effective analyzing power of the NPOL was calculated by Monte Carlo simulation of the experimental setup (see Sec. IV). For the ^{3}H$(p, n)^3$He reaction, typical values for the neutron polarization were 0.39 at $E_n = 2.2$ MeV and 0.45 at $E_n = 3.9$ MeV. For the ^{2}H$(d, n)^3$He reaction, typical values for the neutron polarization were 0.40 at $E_n = 3.9$ MeV and 0.69 at 8.5 MeV.

F. Charged-particle polarimeter

A scattering chamber was installed on the beam line approximately 1 m in front of the neutron production target. It housed a charged-particle polarimeter for proton-beam and deuteron-beam polarimetry based on elastic scattering from ^{4}He. The ^{4}He was contained in a cylindrical cell with Havar foil windows of 2.5×10^{-4} cm thickness. The cell was filled with 1 atm of ^{4}He gas. By use of a sliding O-ring seal the cell could be inserted and retracted from the charged-particle beam without breaking the vacuum. The scattered particles were detected with a pair of standard silicon surface-barrier detectors positioned at angles where the figure of merit was largest. The solid-angle acceptance of these detectors was limited to 0.5 msr by two tantalum collimators.

G. Polarized charged-particle beams

The polarized neutrons needed for the ^{12}C$(n, n)^{12}$C $A_y(\theta)$ measurements were produced by polarization transfer reactions initiated with polarized proton and deuteron beams. These charged-particle beams were delivered by the TUNL ABPIS (Ref. [15]). The polarized ion beam of 80 keV was guided to the chopper and buncher region, which is located at the low-energy side of the tandem accelerator, resulting in beam bursts with a repetition rate of 2.5 MHz. Afterward the ion beam was accelerated by the tandem accelerator to energies required for producing monoenergetic neutron beams in the energy range between 2.2 and 8.5 MeV. The TUNL chopping and bunching system (Ref. [16]) is capable of efficiencies near 60% while producing beam bursts of less than 2 ns FWHM on target. Typical pulsed-ion-beam currents on target in the TUNL NTOF target area ranged from 200 nA at the lowest energy (around 1.3 MeV) used in the present work up to 600 nA at the highest energy (around 5.5 MeV). Typical values for the proton- and deuteron- (vector) beam polarization were 0.63 and 0.75, respectively. To cancel instrumental asymmetries in the charged-particle asymmetry and neutron asymmetry measurements, the polarization direction of the polarized ion beam was inverted from up to down and vice versa (relative to the horizontal scattering plane) at a rate of 10 Hz by use of the eight-step sequence $+ - + + - + - -$, which removes instrumental asymmetries in first and second order [17]. A capacitive time-pickoff unit was installed just in front of the neutron production target to derive a fast timing signal from the pulsed ion beam.

III. DATA ACQUISITION

The general data acquisition techniques used for both the n-^{12}C $A_y(\theta)$ measurements and the NPOL measurements were very similar.

A. Neutron-^{12}C asymmetry measurements

TOF spectra were collected for each of the two main neutron detectors. The start signals for the TOF measurements were generated from the neutron detectors, and the stop signal came from the delayed time-pickoff signal derived from the pulsed ion beam [beam pickoff (BPO)]. The hardware energy threshold for the neutron detectors was set to one-third of the ^{137}Cs Compton edge in the pulse-height spectrum. This corresponds to an effective threshold in the neutron detectors of about $E_n = 0.6$ MeV. Once an event had passed this threshold, the data acquisition code used the "short-gate" pulse height and the "long-gate" pulse height in the neutron detectors to calculate the x-axis and y-axis PSD values. An example of the resulting PSD spectrum is shown in Fig. 2 with a gate set around the neutron events. Only if an event falls into this gate will the associated TOF spectrum be incremented. A typical TOF spectrum is shown in Fig. 3. Time increases from right to

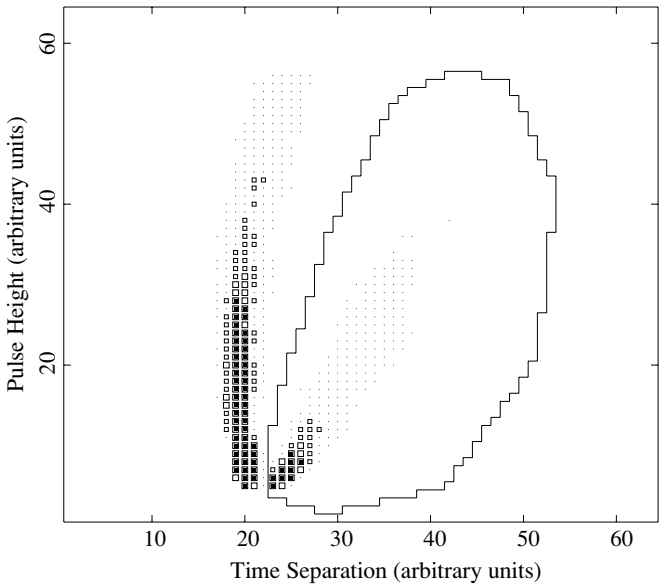

FIG. 2. Typical neutron detector PSD spectrum with a gate set around the neutrons of interest.

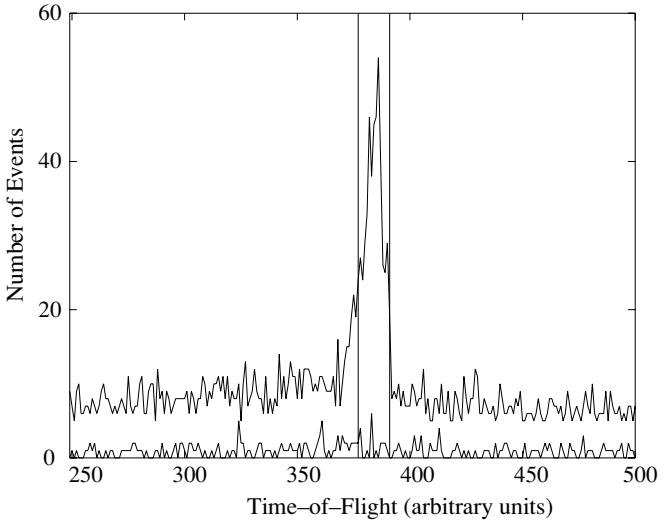

FIG. 3. NTOF spectra at $\theta_{lab} = 65^\circ$ for neutron scattering from carbon at $E_n = 6.0$ MeV. The upper spectrum is with the carbon sample in place. This spectrum has been shifted upward by five counts to show also the spectrum obtained with the carbon sample removed (lower spectrum). Time increases from right to left. The vertical lines indicate the gate used for determining the yield of elastically scattered neutrons.

left. The upper spectrum was obtained with the carbon sample in place. This spectrum has been shifted upward, i.e., five counts were added to the content in each individual channel to make it possible to clearly visualize simultaneously the associated sample-out spectrum, which was obtained with the carbon sample removed (but with the thin support wire in place). The pronounced peak in the sample-in spectrum in the vicinity of channel 380 is due to neutron elastic scattering from carbon nuclei. The "white" neutron component present on both sides of this peak comes from the "sea" of background neutrons in the target room that have lost their time correlation and polarization because of many scatterings from objects in the target room (e.g., the wall, floor, and ceiling). These neutrons produce a flat background in the TOF spectrum. Because of the excellent PSD features of our neutron detectors, γ-ray-induced events are virtually absent in the TOF spectrum shown in Fig. 3. Unfortunately, the peak in the sample-in spectrum is not only due to single scattering from carbon; potentially, it contains events that are due to multiple scattering from carbon, and single and multiple scattering from other objects such as shadow bars, collimators, and air.

The sample-out spectrum contains all of the processes just mentioned, except for those that are due to the presence of the carbon sample. The fact that the sample-out spectrum is primarily composed of "white" neutrons without a pronounced time-correlated component is a clear manifestation that contributions from polarized neutron scattering from shadow bars, collimators, air, etc., are small for our experimental setup. Of course, the sample-out spectrum serves as only an approximate measurement of the background. For example, when the carbon sample is removed, a volume of air replaces it. Therefore the portion of the sample-out spectrum that is due to air scattering is slightly larger than in the sample-in spectrum.

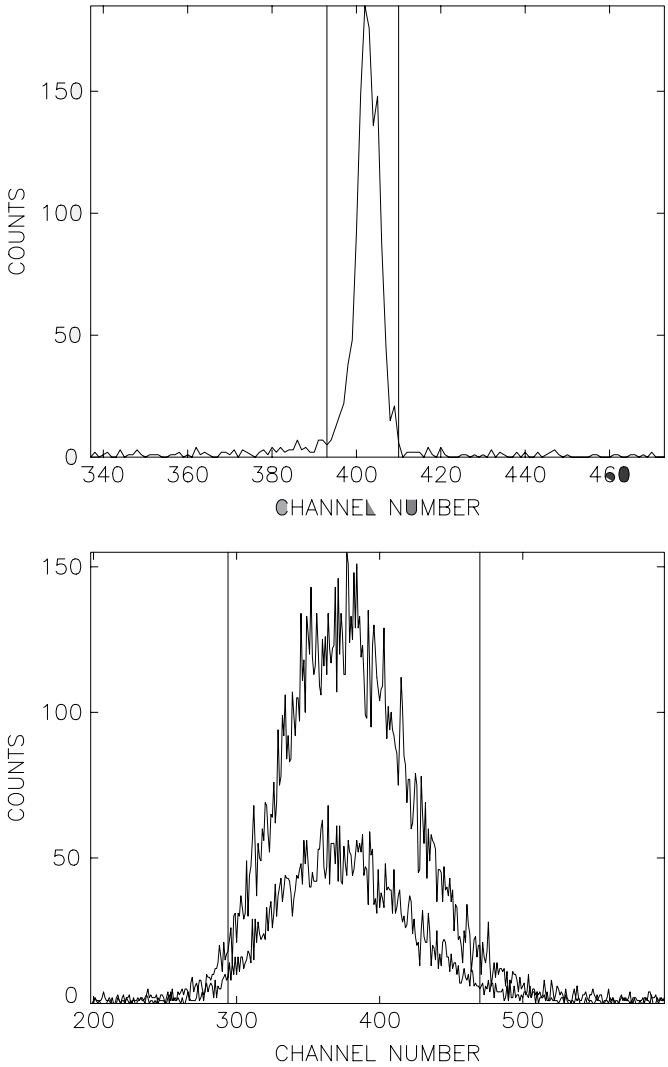

FIG. 4. Top panel: NTOF spectrum for neutron scattering from ^{4}He through 51° (lab) at $E_n = 6.0$ MeV. Time increases from right to left. Bottom panel: ^{4}He recoil-energy spectra (top histogram for neutron spin-up, bottom histogram for neutron spin-down) in the high-pressure He gas scintillator produced by neutrons that fell into the TOF gate shown in the upper panel. The gate shown around the ^{4}He recoil energy is used for the asymmetry determination.

In addition, there are sources of background in the sample-in spectrum that are not present in the sample-out spectrum. For example, after the initial elastic-scattering process from ^{12}C, the neutrons potentially could scatter from the collimator, shadow bars, or air into the detector. Another possibility is scattering first from the shadow bars and then from the carbon sample into the detector. Fortunately, the combination of different flight paths, kinematics, and cross sections of the processes involved greatly reduces these contributions to the time window of interest shown in Fig. 3. The TOF spectra were routed into spin-up and spin-down data areas and sample-in and sample-out data areas, resulting in a total of eight data areas.

Typically, the beam time spent collecting the sample-in data was 2–3 times greater than that for the sample-out data.

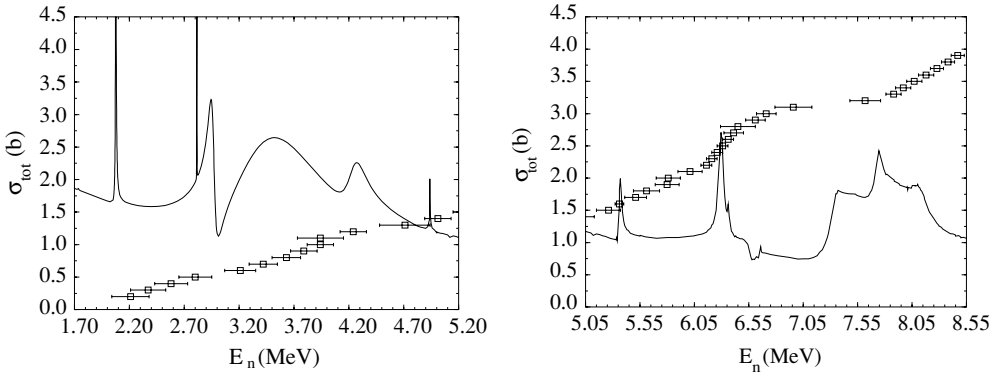

FIG. 5. Energy dependence of n-^{12}C total cross section (solid curve) in comparison with the mean neutron-energies (squares) and associated neutron-energy spread (horizontal bars) of the present n-^{12}C $A_y(\theta)$ measurements. The vertical displacement of the symbols is for reasons of clarity.

Therefore the sample-out spectra were normalized by the ratio of sample-in and sample-out charge deposited in the neutron production target by the incident ion beam. Once normalized, the sample-out spectra were subtracted from the associated sample-in spectra to produce a total of four difference spectra. In most cases the difference spectra were very clean and had only a few counts outside the elastic-scattering peak. However, in some cases there was residual background in the difference spectra. To accurately extract analyzing power data in these cases, it is necessary to know the asymmetry of the remaining background for spin-up and spin-down neutron beams. To deduce information about the asymmetry of the background underneath the peak of interest, the spin-up and spin-down spectra were superimposed and the background levels in the region of interest were compared and computed. For this purpose the background was fitted for each of the four spectra with a constant level and subtracted from the difference spectra to produce the final spectra. The magnitude of the asymmetry of the background was in all cases consistant with zero. Because of the very small amount of remaining background (in most cases $<2\%$ compared with the yield in the elastic peak), its exact polarization could not be determined accurately in this experiment. However, when basically the same experimental setup was used, higher-precision analyzing power data were obtained during the past 30 years at TUNL for nuclei ranging from ^{1}H to ^{208}Pb that clearly showed that the remaining background (except for the part caused by double scattering in the sample) is in fact unpolarized. A gate was set around the elastic peak in the final spectra at about 30% of the maximum peak height (see Fig. 3). This narrow gate reduces the relative multiple-scattering contributions and other time correlated background events. The neutron yields ($Y_{\rm LU}$, $Y_{\rm LD}$, $Y_{\rm RU}$, $Y_{\rm RD}$) extracted from these gates in the final spectra were used to calculate the raw n-^{12}C asymmetry:

$$\epsilon = (\alpha - 1)/(\alpha + 1), \tag{1}$$

where

$$\alpha = [(Y_{\rm LU}Y_{\rm RD})/(Y_{\rm LD}Y_{\rm RU})]^{1/2}. \tag{2}$$

Here, $Y_{\rm LU}$ refers to the left (L) detector and neutron spin in the up (U) orientation, etc.

B. Neutron-^{4}He asymmetry measurements

The only difference between the n-^{12}C and n-^{4}He asymmetry measurements was the fact that the n-^{4}He polarimeter involved an active target, i.e., a ^{4}He high-pressure gas scintillator. This made it possible to record the ^{4}He recoil energy in addition to the TOF information between the BPO and the ^{4}He cell, and between the BPO and the two polarimeter neutron detectors. A gate was set on the neutron peak in the BPO-^{4}He cell TOF spectrum. Only when an event fell into this gate was the BPO-neutron detector TOF spectrum incremented. Subsequently the ^{4}He cell-neutron detector TOF was calculated for scattering to the left-hand or right-hand polarimeter detector and for spin-up and for spin-down conditions. Of course, the event must have satisfied the condition that it fall into the neutron window in the two-dimensional PSD spectrum. The top panel of Fig. 4 shows the NTOF with a gate set on the neutron peak of interest. The bottom panel shows the associated ^{4}He recoil energy for spin-up (upper histogram) and spin-down (lower histogram) for scattering to one of the neutron detectors. The gate indicates the region used for obtaining the yields $Y_{\rm LU}$, $Y_{\rm LD}$, $Y_{\rm RU}$, and $Y_{\rm RD}$ from which the raw n-^{4}He asymmetry was calculated with Eqs. (1) and (2).

IV. FINITE-GEOMETRY AND MULTIPLE-SCATTERING CORRECTIONS

The measured raw n-^{12}C (n-^{4}He) asymmetry is the asymmetry averaged over the solid angles subtended by the neutron production target, the carbon scatterer (^{4}He gas scintillator), and the main (polarimeter) neutron detectors. In addition, the measured asymmetries contain events from various multiple-scattering processes. The effects of finite geometry and multiple scattering manifest themselves as low-energy tails on the left-hand side of the peaks in the NTOF spectra (see Figs. 3 and 4). Furthermore, the effective scattering angle is not identical to the nominal angle at which the detectors were positioned because of neutron flux attenuation in the carbon sample (^{4}He gas scintillator) and the variation of the differential cross section $\sigma(\theta)$ across the solid angle

of the carbon sample (^{4}He gas scintillator). In general, the net effect of finite geometry and multiple scattering is a decrease in the measured asymmetry from its point-geometry single-scattering value. Corrections had to be calculated to compensate for the effects of finite geometry and multiple scattering.

A. Neutron-^{4}He Monte Carlo corrections

The corrections for the effects of finite geometry and multiple scattering were calculated by Monte Carlo simulation of the experimental setup [1,13]. To calculate the effective analyzing power $\bar{A}_y$ of the polarimeter, the n-^{4}He phase shifts of Stammbach and Walter [12] were used. The relative uncertainty in the $\bar{A}_y$ generated by these phase shifts was estimated to be $\pm 1\%$. The statistical error that was due to the Monte Carlo simulations was negligible. The multiple-scattering corrections compensated for the effects of the following possible neutron double-scattering processes: He-He, He-Xe, Xe-He, He-Fe, and Fe-He. The cross-section and analyzing power values for neutron scattering from Xe and Fe were based on experimental data or were calculated from published optical-model parameters. Single-scattering events from nonhelium materials were experimentally not detected and therefore can be ignored. Triple-scattering events were negligible.

Tables I and II summarize the results of the Monte Carlo simulations, the measured n-^{4}He asymmetry, and the deduced neutron polarization values obtained for the n-^{12}C asymmetry measurements conducted with the ^{3}H$(p,n)^3$He (see Table I) and ^{2}H$(d,n)^3$He (see Table II) reaction, respectively. Here, the neutron polarization P_n and its uncertainty ΔP_n were calculated from the equations

$$P_n = \epsilon / \bar{A}_y \tag{3}$$

and

$$\Delta P_n = (\epsilon/\bar{A}_y)[(\Delta \bar{A}_y/\bar{A}_y)^2 + (\Delta\epsilon/\epsilon)^2]^{\frac{1}{2}}, \tag{4}$$

where ϵ is the measured asymmetry.

B. Neutron-^{12}C Monte Carlo corrections

The corrections were calculated with the Monte Carlo code JANE [18], which was written to correct analyzing power data measured with NTOF spectroscopy. The code simulates the experimental setup by using $\sigma(\theta)$ and $A_y(\theta)$ libraries to model the neutron interaction for single and multiple scattering. It calculates TOF spectra and applies a gate around the elastic-scattering TOF peak as was done in the analysis of the experimental n-^{12}C data. From the yields in these gates and the P_n values from Sec. IV A it calculates the analyzing power in n-^{12}C scattering. The correctness of the Monte Carlo results depends primarily on the accuracy of the $A_y(\theta)$ library values and to a lesser extent on the $\sigma(\theta)$ library values. The $\sigma(\theta)$ and $A_y(\theta)$ libraries were composed of values produced by expansion of $\sigma(\theta)$ in Legendre polynomials and the product $\sigma(\theta)A_y(\theta)$ in associated Legendre polynomials, respectively. The A_y library values were produced from the present uncorrected $A_y(\theta)$ values combined with evaluations of previous measurements. The process for using JANE is an iterative procedure. In the second iteration results from the first iteration are again used in an associated Legendre polynomial fit. This fit is then used to produce $A_y(\theta)$ values to update the input library. Successive iterations are performed until

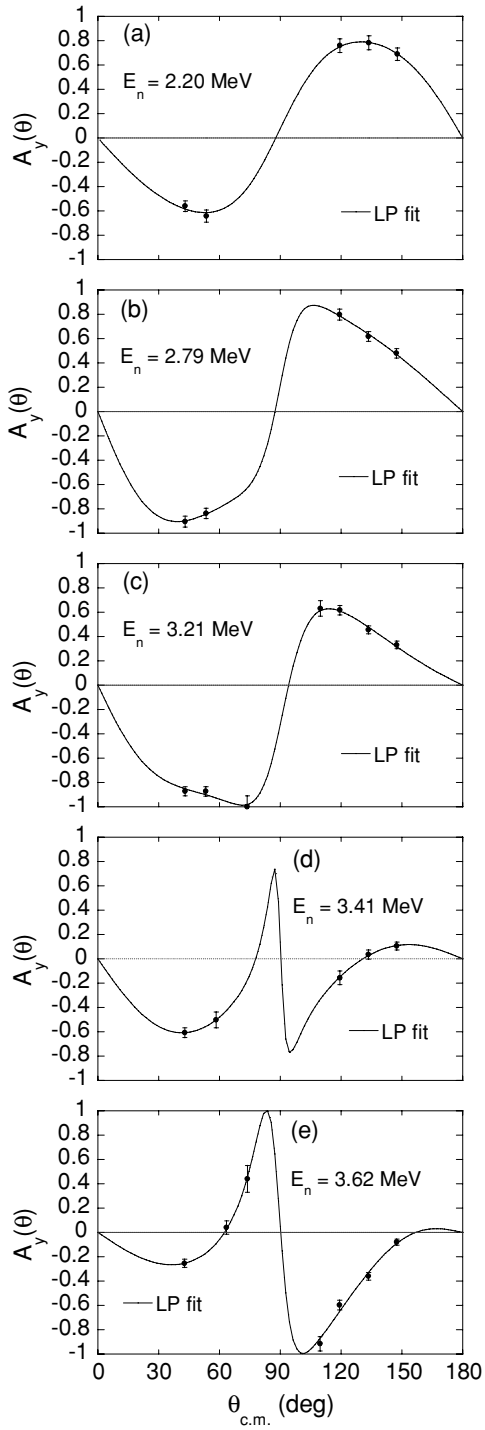

FIG. 6. Present n-^{12}C $A_y(\theta)$ data (dots) and associated Legendre polynomial fits for E_n between 2.20 and 3.62 MeV.

TABLE I. Results of the neutron polarimetry analysis for the n-^{12}C $A_y(\theta)$ measurements obtained with the ^{3}H$(\vec{p},\vec{n})$ neutron source reaction. The columns are from left to right, the neutron-energy at the midpoint of the gas cell, neutron-energy spread, single-scattering point-geometry $A_y(\theta)$ values for ^{4}He$(\vec{n},n)$ scattering, Monte Carlo $A_y(\theta)$ results for finite geometry (fg) and finite geometry with multiple scattering (fgms), cumulative measured asymmetry, statistical error, and the cumulative neutron polarization ever, and statistical error. Here, $A_y^{\rm fgms}$ stands for the effective analyzing power $\bar{A}_y$.

$E_n^{\rm mid}$	$E_n^{\rm sprd}$	$A_y^{\rm pg}$	$A_y^{\rm fg}$	$A_y^{\rm fgms}$	ε	$\pm\Delta\varepsilon$	P_n	$\pm\Delta P_n$
2.21	0.17	−0.231	−0.224	−0.222	0.087	±0.003	0.390	±0.014
2.37	0.16	−0.287	−0.280	−0.277	0.103	±0.007	0.372	±0.027
2.58	0.15	−0.352	−0.343	−0.340	0.120	±0.009	0.352	±0.025
2.80	0.15	−0.409	−0.399	−0.394	0.146	±0.004	0.371	±0.009
3.21	0.14	−0.500	−0.490	−0.485	0.194	±0.004	0.400	±0.008
3.42	0.13	−0.541	−0.530	−0.525	0.209	±0.007	0.397	±0.013
3.63	0.13	−0.576	−0.564	−0.558	0.240	±0.005	0.431	±0.009
3.79	0.12	−0.597	−0.585	−0.578	0.247	±0.007	0.428	±0.012
3.94	0.12	−0.614	−0.602	−0.595	0.265	±0.009	0.446	±0.016

TABLE II. Results of the neutron polarimetry analysis for the n-^{12}C $A_y(\theta)$ measurements obtained with the ^{2}H$(\vec{d},\vec{n})$ neutron source reaction. The columns consist of neutron-energy at the midpoint of the gas cell, neutron-energy spread, point-geometry $A_y(\theta)$ values for ^{4}He$(\vec{n},n)$ scattering, Monte Carlo $A_y(\theta)$ results for finite geometry (fg) and finite geometry with multiple scattering (fgms), cumulative measured asymmetry error, statistical error, the cumulative neutron polarization error, and statistical error. Here, $A_y^{\rm fgms}$ stands for the effective analyzing power $\bar{A}_y$.

$E_n^{\rm mid}$	$E_n^{\rm sprd}$	$A_y^{\rm pg}$	$A_y^{\rm fg}$	$A_y^{\rm fgms}$	ε	$\pm\Delta\varepsilon$	P_n	$\pm\Delta P_n$
3.94	0.21	0.613	0.599	0.593	0.235	±0.007	0.396	±0.012
4.24	0.12	0.639	0.614	0.608	0.275	±0.010	0.452	±0.016
4.71	0.23	0.660	0.643	0.636	0.309	±0.006	0.486	±0.009
5.01	0.12	0.663	0.647	0.640	0.350	±0.005	0.547	±0.008
5.26	0.11	0.662	0.650	0.643	0.358	±0.008	0.556	±0.012
5.36	0.04	0.661	0.647	0.640	0.385	±0.011	0.602	±0.017
5.51	0.10	0.659	0.641	0.634	0.365	±0.006	0.576	±0.010
5.61	0.12	0.657	0.645	0.638	0.407	±0.006	0.638	±0.009
5.80	0.11	0.652	0.633	0.626	0.379	±0.006	0.605	±0.010
5.81	0.11	0.652	0.633	0.626	0.432	±0.012	0.666	±0.016
6.01	0.11	0.646	0.628	0.621	0.420	±0.004	0.677	±0.007
6.16	0.05	0.641	0.624	0.617	0.423	±0.008	0.686	±0.013
6.21	0.05	0.640	0.622	0.615	0.418	±0.008	0.680	±0.013
6.26	0.05	0.638	0.619	0.611	0.414	±0.008	0.678	±0.013
6.31	0.05	0.636	0.617	0.611	0.416	±0.010	0.682	±0.016
6.36	0.05	0.635	0.621	0.614	0.411	±0.009	0.670	±0.014
6.41	0.09	0.633	0.622	0.615	0.427	±0.005	0.694	±0.009
6.45	0.16	0.632	0.619	0.612	0.405	±0.008	0.660	±0.013
6.61	0.09	0.626	0.609	0.603	0.418	±0.006	0.694	±0.011
6.71	0.09	0.622	0.604	0.598	0.404	±0.006	0.676	±0.011
6.96	0.17	0.613	0.595	0.589	0.416	±0.003	0.707	±0.006
7.62	0.14	0.588	0.574	0.568	0.406	±0.003	0.714	±0.005
7.88	0.07	0.579	0.562	0.556	0.395	±0.004	0.711	±0.007
7.97	0.07	0.576	0.559	0.553	0.396	±0.004	0.716	±0.007
8.07	0.07	0.572	0.552	0.546	0.390	±0.004	0.714	±0.007
8.18	0.07	0.569	0.549	0.544	0.390	±0.008	0.717	±0.014
8.28	0.06	0.565	0.547	0.541	0.394	±0.006	0.728	±0.012
8.38	0.06	0.562	0.544	0.538	0.387	±0.006	0.719	±0.012
8.47	0.06	0.558	0.541	0.535	0.386	±0.007	0.722	±0.012

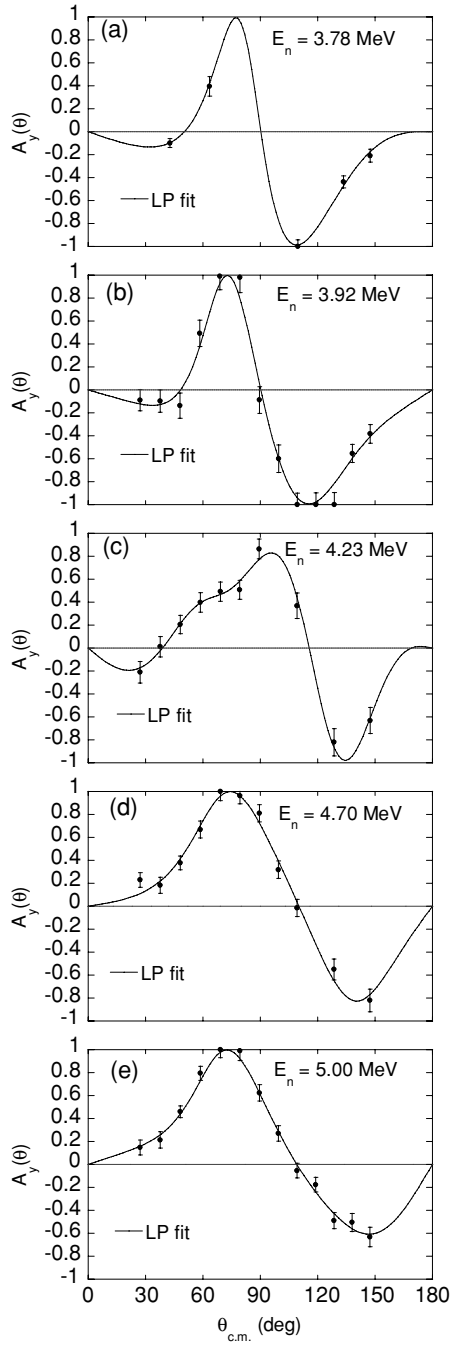

FIG. 7. Same as Fig. 6 but for E_n between 3.78 and 5.00 MeV.

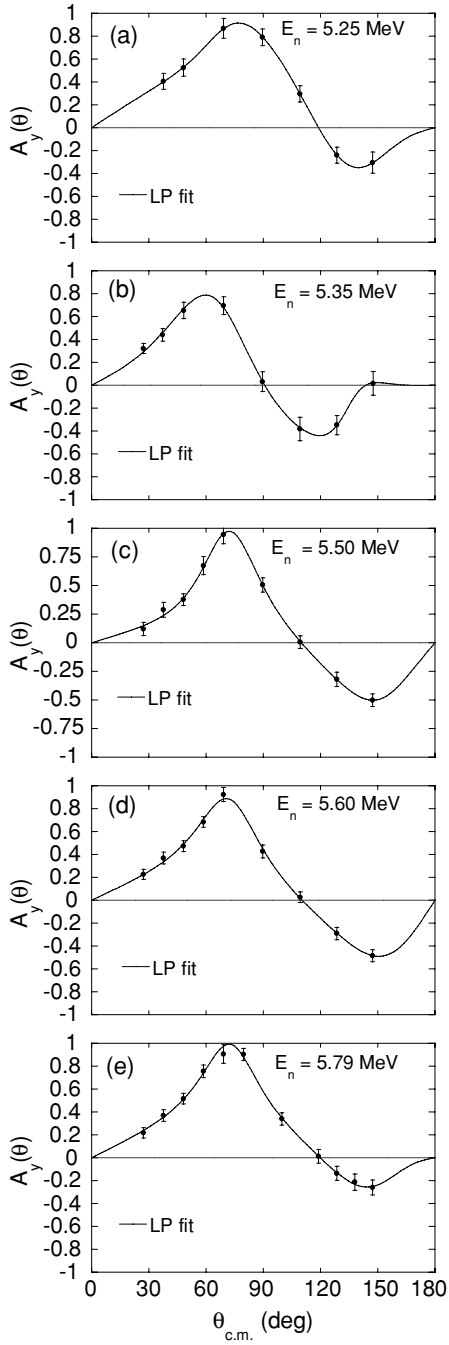

FIG. 8. Same as Fig. 6 but for E_n between 5.25 and 5.79 MeV.

satisfactory convergence is achieved. For most cases, only three iterations were needed.

V. RESULTS

The solid curve in Fig. 5 is a fit to the n-^{12}C total cross-section data in the energy range of interest. The squares indicate the energies, and the width of the horizontal bars represents the energy spread associated with the present n-^{12}C $A_y(\theta)$ data. As can be seen, the energy region between 2.2 and 8.5 MeV is almost completely covered, except for $E_n = 3.0$ MeV and $E_n = 4.4$ MeV, and the neutron-energy range from 7.10 to 7.50 MeV. From the phase-shift analysis (PSA) of Galati, Brandenberger, and Weil (hereafter GBW) [19] it is known that at these three energy regions $A_y(\theta)$ varies rapidly with neutron-energy. Considering our finite neutron-energy spread, it would have been impossible to extract useful $A_y(\theta)$ information at these energies.

Figures 6–12 show the present n-^{12}C $A_y(\theta)$ data. The solid curves are based on fits to the product of $A_y(\theta)$ and $\sigma(\theta)$ obtained with associated Legendre polynomials and are

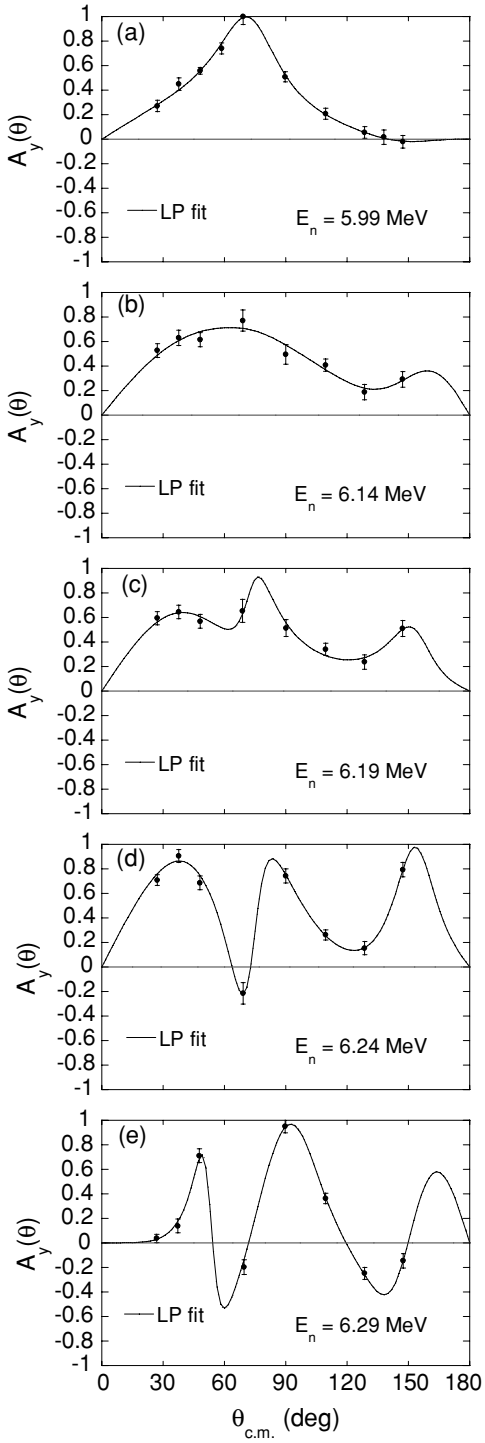

FIG. 9. Same as Fig. 6 but for E_n between 5.99 and 6.29 MeV.

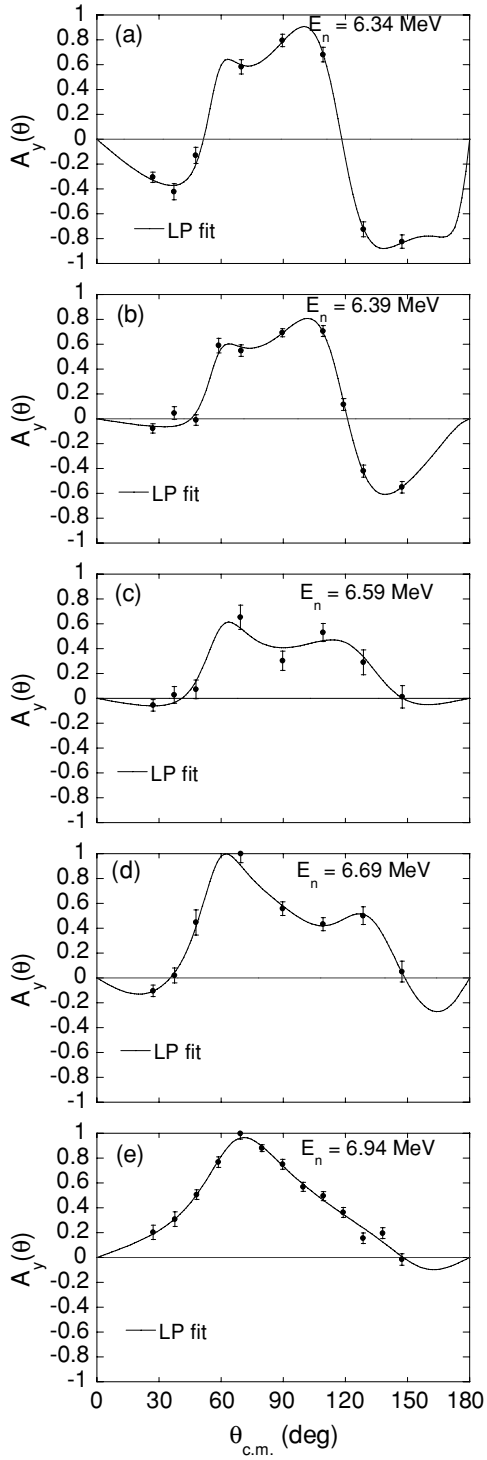

FIG. 10. Same as Fig. 6 but for E_n between 6.34 and 6.94 MeV.

intended to guide the eye. Figures 13–17 compare the present n-^{12}C $A_y(\theta)$ data with published data and with the results of previous PSAs. In these figures we often show two curves at slightly different energies to indicate the energy sensitivity of the PSA results. As can be seen from Fig. 13(a), our data (filled circles) at $E_n = 2.20$ MeV are in good agreement with the data of Holt *et al.* [20] at $E_n = 2.20$ and 2.30 MeV and with the old PSA result of Ref. [21] obtained from fits to the data of Drigo *et al.* [22], Knox *et al.* [23], and Lane, Koshel, and Monahan [24] for neutron energies below 3 MeV. The simple sinusoidal shape observed for $A_y(\theta)$ at $E_n = 2.20$ MeV continues to dominate also at $E_n = 2.79$ MeV [Fig. 13(b)]. Here, the present data are in excellent agreement with previous data and the PSA result of Ref. [21]. It is gratifying to see that

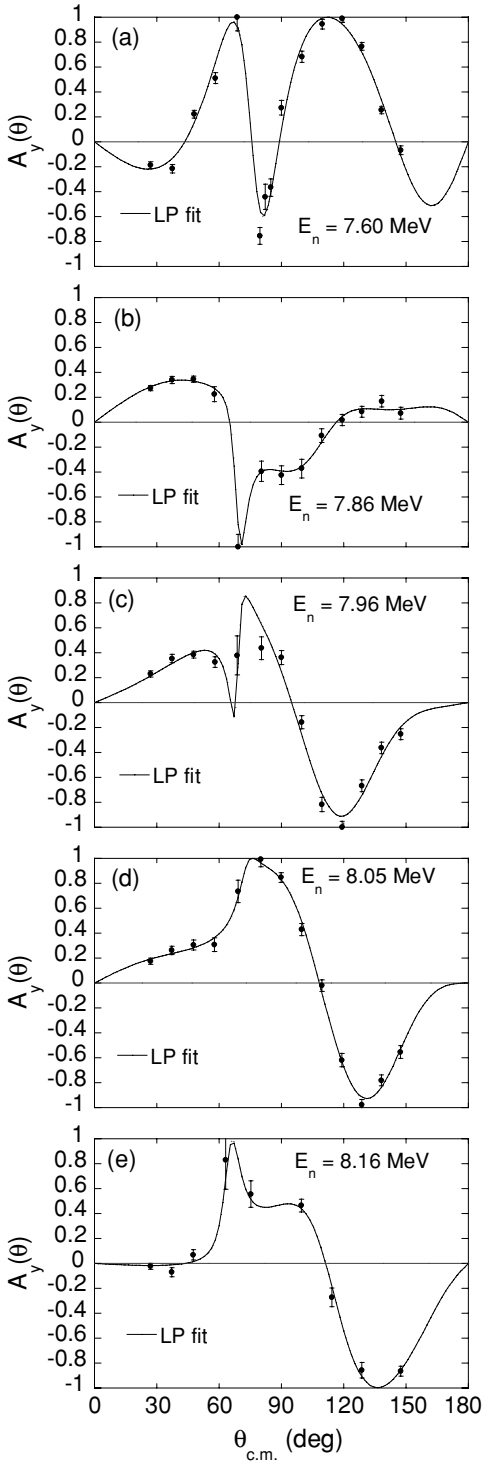

FIG. 11. Same as Fig. 6 but for E_n between 7.60 and 8.16 MeV.

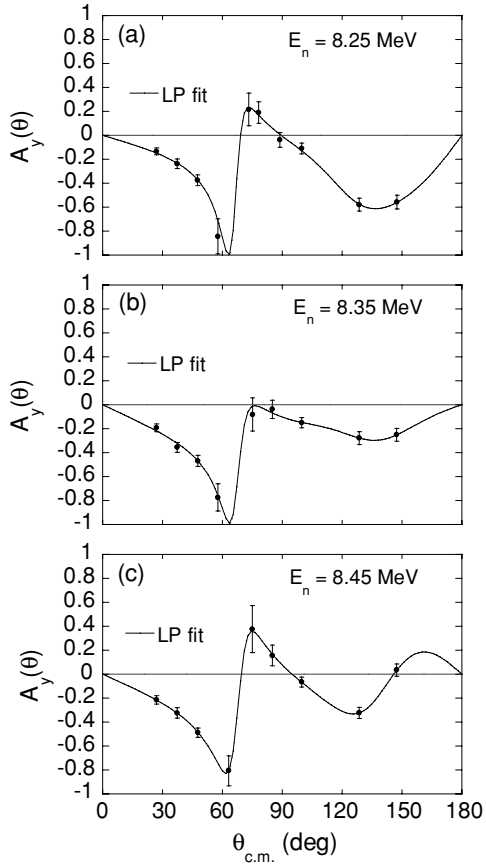

FIG. 12. Same as Fig. 6 but for E_n between 8.25 and 8.45 MeV.

the PSA of GBW *et al*. [19] is also in good agreement with our $A_y(\theta)$ data at $E_n = 3.21$ MeV [Fig. 13(c)] and 3.62 MeV [Fig. 13(d)]. This PSA covers the neutron-energy range from 3.0 to 7.0 MeV. At $E_n = 3.92$ MeV our data [Fig. 14(a)] clearly support GBW and the data of Drigo *et al*. The backward-angle data of Gorlov, Lebedeva, and Morozov [25] appear to be incorrect. Because of the resonance structure at $E_n = 4.3$ MeV (see Fig. 5) $A_y(\theta)$ predicted by GBW changes rapidly between 4.20 and 4.30 MeV in the angular range between $\theta = 70^\circ$ and 130° c.m. [Fig. 14(b)]. Our data at $E_n = 4.23$ MeV are in better agreement with the GBW results at 4.30 MeV than at 4.20 MeV. Considering our uncertainty in the absolute neutron-energy scale and the one of GBW (± 5 keV in either case), this observation may not be surprising. The GBW results at $E_n = 4.30$ and 4.40 MeV are in close agreement with each other. Therefore the agreement of the present data at $E_n = 4.23$ MeV with those of Drigo *et al*. at $E_n = 4.40$ MeV is not unexpected. At $E_n = 4.70$ MeV [Fig. 14(c)] our data are in reasonably good agreement with the previous data of Drigo *et al*. and Holt *et al*. and the GBW results. At $E_n = 5.00$ MeV [Fig. 14(d)] our forward- and backward-angle results do not support the GBW results. This tendency continues at $E_n = 5.25$ MeV [Fig. 15(a)], where our data define $A_y(\theta)$ much better than the previous data of Drigo *et al*. at $E_n = 5.20$ MeV. In fact, at $E_n = 5.25$ MeV our data deviate considerably from the GBW results throughout almost the entire angular range investigated. Over the narrow resonance at $E_n = 5.35$ MeV (see Fig. 5) the predictions of GBW for $A_y(\theta)$ change dramatically with neutron-energy for backward angles [see Fig. 15(b)]. Therefore, considering our total neutron-energy spread of 100 keV, our results at $E_n = 5.35$ MeV are in excellent agreement with those of GBW. In the neutron-energy range between 5.5 and 6.0 MeV [Figs. 15(c) and 15(d)] our data

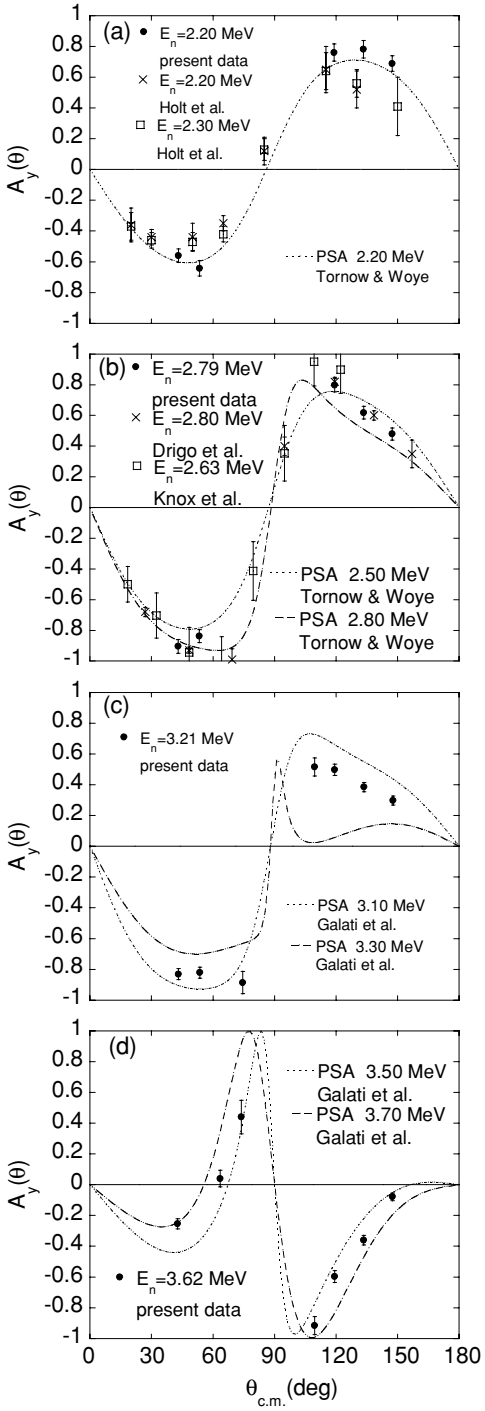

FIG. 13. Present n-^{12}C $A_y(\theta)$ data (filled circles) in comparison with previous data and PSA predictions for E_n between 2.20 and 3.62 MeV.

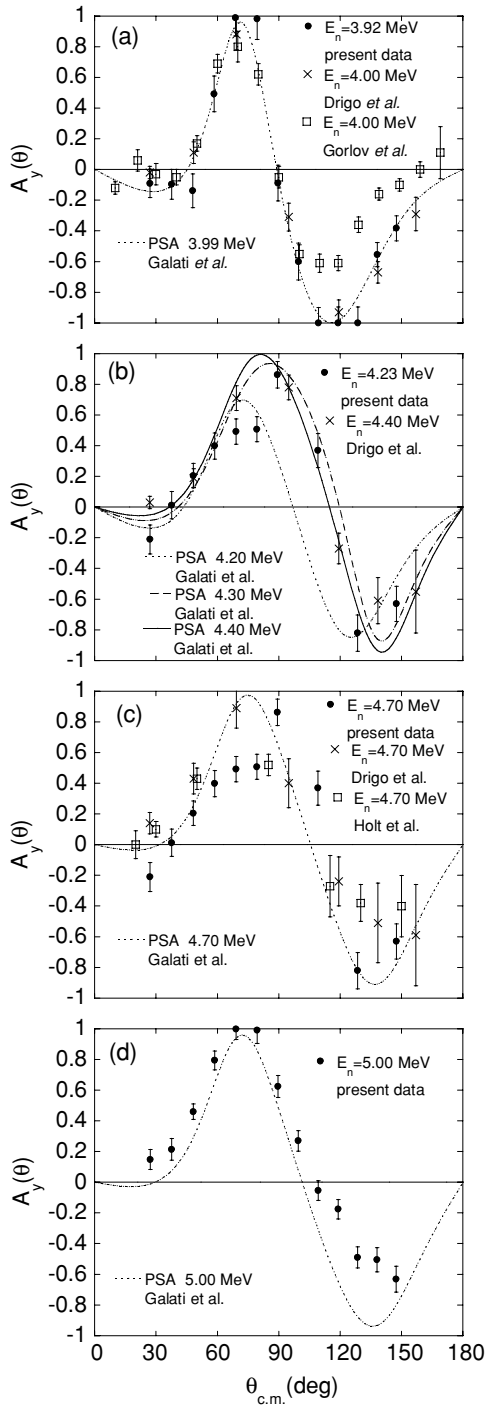

FIG. 14. Same as Fig. 13 but for E_n between 3.92 and 5.00 MeV.

do not support the GBW predictions. Although the shape is about right, the magnitude of $A_y(\theta)$ is incorrect. This may not be too surprising because $A_y(\theta)$ data were not available in this energy range when the PSA of GBW was performed.

Across the $E_n = 6.3$ MeV resonance seen in the n-^{12}C total cross section (see Fig. 5), both the predicted and measured $A_y(\theta)$ vary dramatically with energy [see Figs. 16(a)–16(c)], and our data are in considerable disagreement with the GBW predictions. This disagreement continues at $E_n = 6.59$ MeV [Fig. 16(d)] and $E_n = 6.94$ MeV [Fig. 17(a)], the upper end of the predictions of GBW. The PSA prediction of Chen and Tornow [26] (in the following text referred to as CT) is in good agreement with our data at $E_n = 6.94$ MeV. As can be seen from the n-^{12}C total cross section (see Fig. 5), the

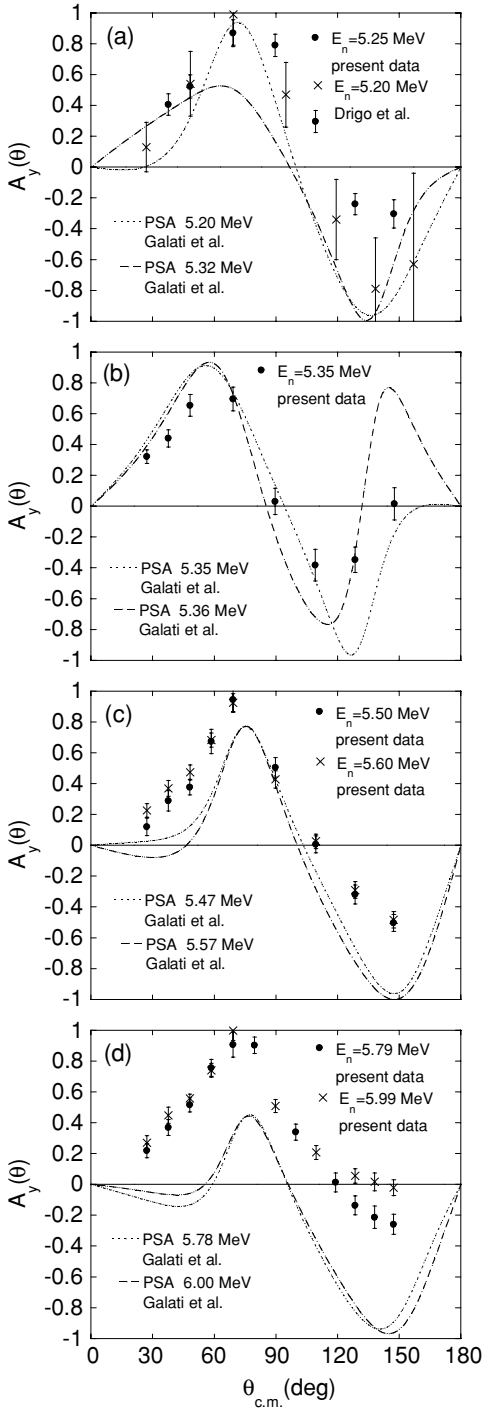

FIG. 15. Same as Fig. 13 but for E_n between 5.25 and 5.79 MeV.

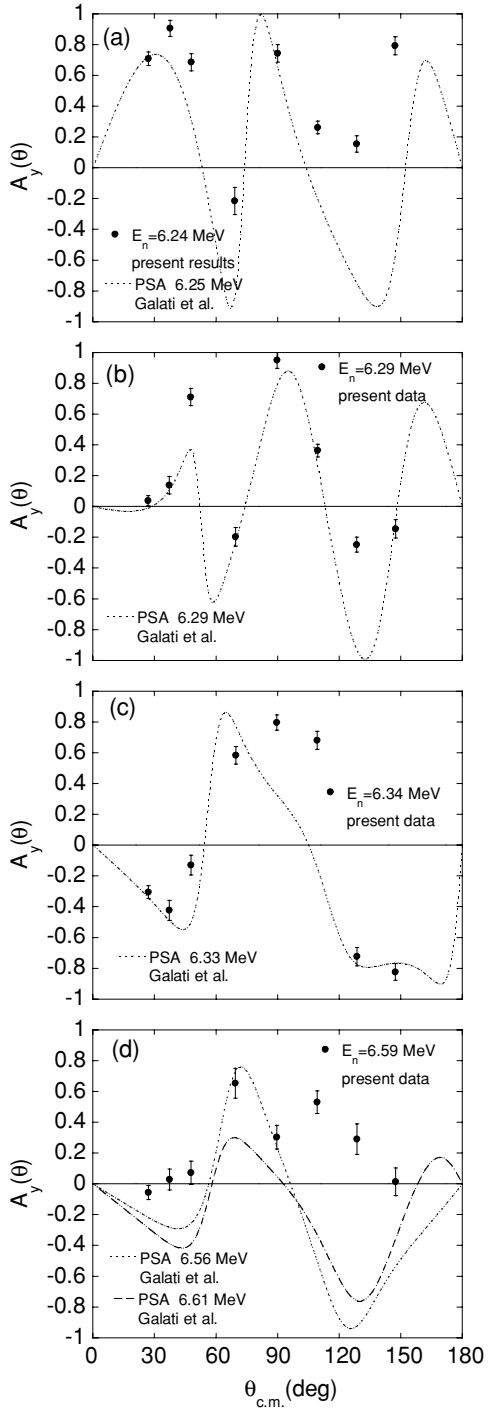

FIG. 16. Same as Fig. 13 but for E_n between 6.24 and 6.59 MeV.

energy range between 7.2 and 8.3 MeV is characterized by a number of overlapping resonances [27]. Therefore one expects $A_y(\theta)$ to vary strongly with energy. Figures 17(b)–17(d) and 18(a)–18(d) support this conjecture. The $A_y(\theta)$ predicted by CT at $E_n = 7.60$ MeV [Fig. 17(b)] is in fair agreement with our data at this energy, except at angles forward of 60°, where the CT solution at $E_n = 7.70$ MeV provides a better representation of the data. However, in the angular range between 80° and 100°, the $E_n = 7.70$ MeV CT solution is out of phase with the data. At $E_n = 7.86$ MeV [Fig. 17(c)] CT misses the data completely, although the shape of the $E_n = 7.90$ MeV solution resembles the shape of the data. At 8.05 MeV [Fig. 17(d)] the CT solution at $E_n = 8.00$ MeV describes the forward-angle data very well, whereas it fails considerably for angles beyond 70°. The $E_n = 8.10$ MeV solution shows exactly the opposite behavior. Between $E_n = 8.16$ and 8.25 MeV [Figs. 18(a) and 18(b)] the data continue to vary strongly with energy. The CT predictions miss the forward-angle data at $E_n = 8.16$ MeV

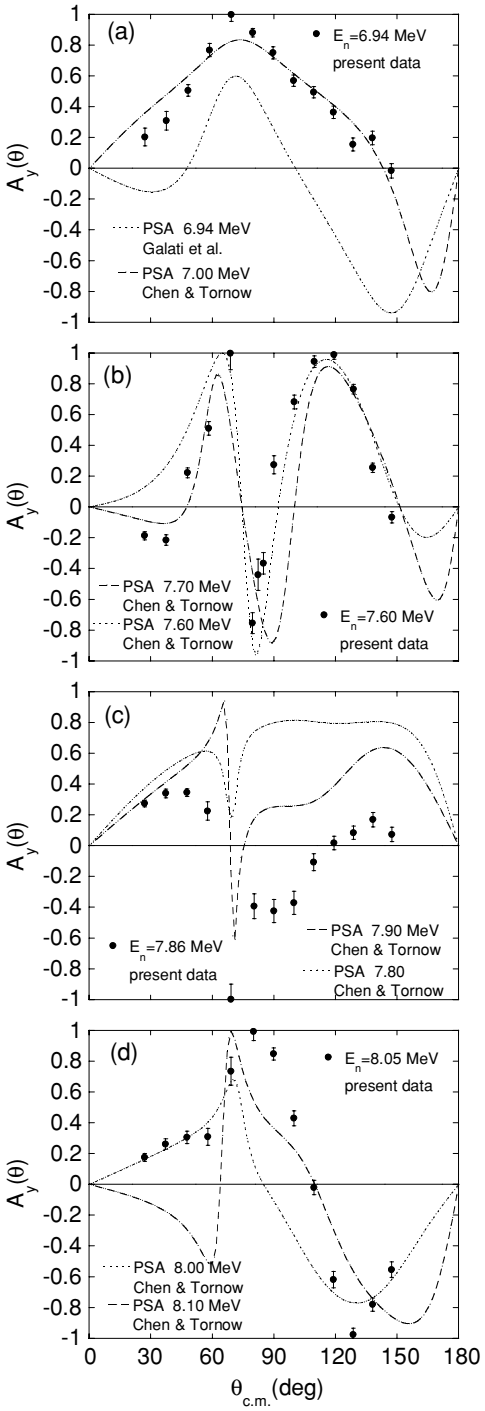

FIG. 17. Same as Fig. 13 but for E_n between 6.94 and 8.05 MeV.

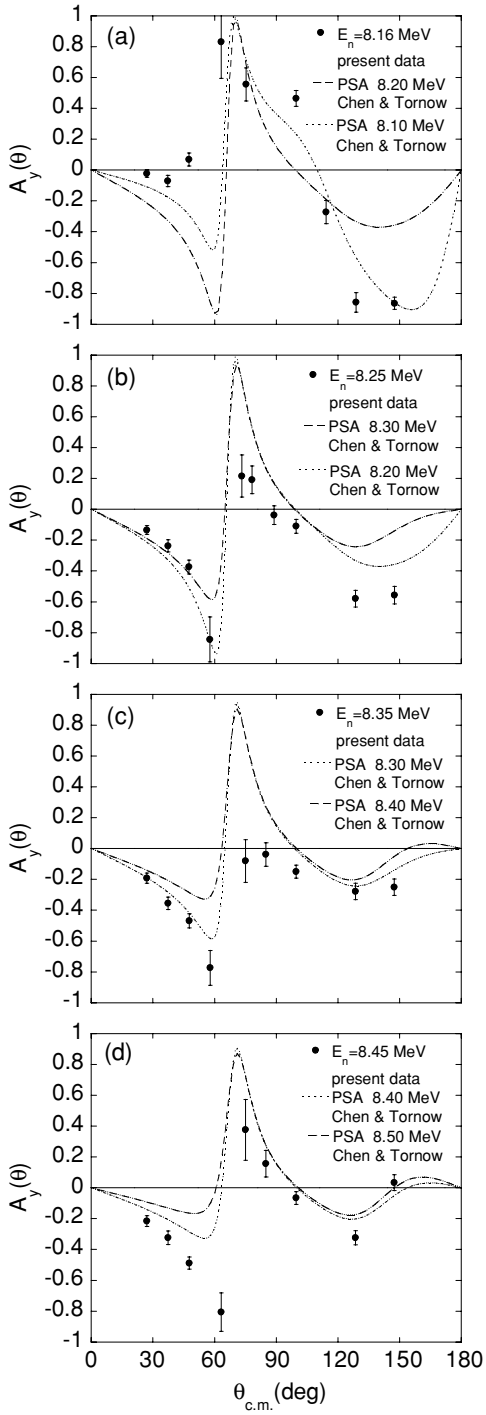

FIG. 18. Same as Fig. 13 but for E_n between 8.16 and 8.45 MeV.

whereas at $E_n = 8.25$ they are reasonably well described. Between $E_n = 8.25$ and 8.45 MeV the CT solutions vary smoothly with energy, as do the data [Figs. 18(b)–18(d)]. However, the overall agreement between data and calculations is unsatisfactory in this energy range. Although not shown in Figs. 17 and 18, the 1983 PSA of Tornow [27] performed in the narrow energy range from 7.0 to 8.6 MeV gives a better description of the present experimental data than that found by CT between 7.8 and 8.2 MeV.

VI. SUMMARY AND CONCLUSION

The analyzing power $A_y(\theta)$ for $^{12}\mathrm{C}(n,n)^{12}\mathrm{C}$ has been measured for 33 neutron energies ranging from 2.2 to 8.5 MeV. The data for $E_n < 4.7$ MeV are in good agreement with previous measurements and PSA predictions. However, for E_n from 4.7 to 7.0 MeV, for which very little published $A_y(\theta)$ exist, comparisons show that the $A_y(\theta)$ predictions based on available PSAs do not provide an acceptable

description of the present results. For E_n from 7.0 to 8.5 MeV, the present data are consistent with the few previous measurements, but are in rather poor agreement with PSA predictions from 7.9 to 8.5 MeV. The comparisons with published PSA predictions show that a new description of $A_y(\theta)$ from 4.7 to 8.5 MeV is needed. Only then will it be possible to (i) describe n-^{12}C elastic scattering in a consistent way up to about $E_n = 20$ MeV, (ii) obtain accurate information on the ^{13}C level structure in the excitation energy range from $E_x = 8$ to 12 MeV, and (iii) accurately correct very precise, low-energy neutron-proton A_y (data) for false asymmetries caused by the polarization-dependent efficiency of commonly used neutron detectors constructed with organic materials.

ACKNOWLEDGMENTS

This work was supported in part by the U.S. Department of Energy, Office of Nuclear Physics, under grant no. DE-FG02-97ER41033, the U.S. National Science Foundation under grant no. INT-9215354 (U.S.-China Cooperative Science Program), and the National Natural Science Foundation of China.

[1] W. Tornow, H. Spiegelhauer, and G. Mack, Nucl. Instrum. Methods **125**, 373 (1975).
[2] D. Holslin, J. McAninch, P. A. Quin, and W. Haeberli, Bull. Am. Phys. Soc. **32**, 1057 (1987).
[3] W. Tornow, C. R. Howell, M. L. Roberts, P. D. Felsher, Z. M. Chen, R. L. Walter, G. Mertens, and I. Slaus, Phys. Rev. C **37**, 2326 (1988).
[4] D. Holslin, J. McAninch, P. A. Quin, and W. Haeberli, Phys. Rev. Lett. **61**, 1561 (1988).
[5] G. J. Weisel, W. Tornow, C. R. Howell, P. D. Felsher, M. AlOhali, Z. P. Chen, R. L. Walter, J. M. Lambert, P. A. Treado, and I. Slaus, Phys. Rev. C **46**, 1599 (1992).
[6] G. Hale, to be submitted for publication.
[7] Zhenpeng Chen, to be submitted for publication.
[8] P. P. Guss, R. C. Byrd, C. E. Floyd, C. R. Howell, K. Murphy, G. Tungate, R. S. Pedroni, R. L. Walter, J. P. Delaroche, and T. B. Clegg, Nucl. Phys. **A438**, 187 (1985).
[9] J. E. Simmons, W. B. Broste, T. R. Donoghue, R. C. Haight, and J. C. Martin, Nucl. Instrum. Methods **106**, 477 (1973).
[10] P. W. Lisowski, R. L. Walter, C. E. Bush, and T. B. Clegg, Nucl. Phys. **A242**, 298 (1975).
[11] Hamilton Precision Metals, Lancaster, PA.
[12] T. Stammbach and R. L. Walter, Nucl. Phys. **A180**, 225 (1972).
[13] W. Tornow, Z. Phys. **226**, 357 (1974).
[14] A. J. Mendez, C. D. Roper, J. D. Dunham, and T. B. Clegg, Rev. Sci. Instrum. **67**, 3073 (1996).
[15] T. B. Clegg *et al*., Nucl. Instrum. Methods Phys. Res. A **357**, 200 (1995).
[16] S. A. Wender, C. E. Floyd, T. B. Clegg, and W. R. Wylie, Nucl. Instrum. Methods **174**, 341 (1980).
[17] J. E. Koster, E. D. Davis, C. R. Gould, D. G. Haase, N. R. Roberson, L. W. Seagondollar, S. Wilburn, and X. Zhu, Phys. Lett. **B267**, 23 (1991).
[18] E. Woye *et al*., Nucl. Phys. **A394**, 139 (1983).
[19] W. Galati, J. D. Brandenberger, and J. L. Weil, Phys. Rev. C **5**, 1508 (1972).
[20] R. J. Holt, F. W. Firk, R. Nath, and H. L. Schulz, Nucl. Phys. **A213**, 147 (1973).
[21] W. Tornow and E. Woye, University of Tübingen, 1980 (unpublished).
[22] L. Drigo, C. Manduchi, G. Moschini, M. T. Russo Manduchi, C. Tornielli, and G. Zannoni, Nucl. Phys. **A181**, 177 (1972).
[23] H. D. Knox, J. M. Cox, R. W. Finlay, and R. O. Lane, Nucl. Phys. **A217**, 611 (1973).
[24] R. O. Lane, R. D. Koshel, and J. E. Monahan, Phys. Rev. **188**, 1618 (1969).
[25] G. V. Gorlov, N. S. Lebedeva, and V. M. Morozov, Sov. Phys. Dokl. **158**, 574 (1964).
[26] Zhenpeng Chen and W. Tornow, submitted to J. Phys. G: Nucl. Phys.
[27] W. Tornow, J. Phys. G: Nucl. Phys. **9**, 1507 (1983).